Journal of Magnetism and Magnetic Materials 648 (2026) 174081

Contents lists available at ScienceDirect

Journal of Magnetism and Magnetic Materials

journal homepage: www.elsevier.com/locate/jmmm

Research article

Synthesis and properties of NiCo crossed nanotube networks

Joaquín de la Torre Medina [a],*, Pascal Van Velthem [b], Tristan da Câmara Santa Clara Gomes [b,c], Flavio Abreu Araujo [b], Luc Piraux [b]

[a] Instituto de Investigaciones en Materiales - Unidad Morelia, Universidad Nacional Autónoma de México, Antigua Carretera a Pátzcuaro No. 8701 Col. Ex Hacienda de San José de la Huerta, C. P. 58190, Morelia, Mexico

[b] Institute of Condensed Matter and Nanosciences, Université catholique de Louvain, Place Croix du Sud 1, B-1348, Louvain-la-Neuve, Belgium

[c] Instituto de Engenharia de Sistemas e Computadores – Microsistemas e Nanotecnologias (INESC MN) Lisbon, Portugal

ARTICLE INFO

Keywords:
NiCo crossed nanotubes
Ferromagnetic resonance
Magnetic properties
Anisotropic magnetoresistance

ABSTRACT

This paper reports on the synthesis and the characterization of magnetic and magneto-transport properties of electrically interconnected $Ni_{1-x}Co_x$ alloy crossed nanotube networks. The alloy nanotube networks have been fabricated by an adapted electrochemical technique based on a dealloying method previously used for the fabrication of pure Ni nanotubes. Here, we demonstrate that this synthesis approach can be adapted to fabricate NiCo alloy nanotubes with Co contents (x) up to 27%. Increasing the Co content within this range has revealed an increase in the nanotube walls that is accompanied by an increase in the effective magnetic anisotropy, which is attributed to a reinforcement of the magnetostatic field along the nanotube axis. Magneto-transport measurements are consistent with the typical behavior observed previously in magnetic nanotubes, where the dominant magnetization reversal process involves the propagation of vortex-like domain walls. Furthermore, the field position of the drop in resistance close to zero field is consistent with the coercive field, which depends on the nanotube material and wall thickness. The possibility of synthesizing complex electrically interconnected nanoarchitectures, such as crossed nanotube networks made of various ferromagnetic materials, using electrochemical deposition techniques is of particular interest for the development of potential applications in magnetic sensing devices, neuromorphic computing, and spintronics.

1. Introduction

Nowadays, the development of three-dimensional (3D) nanoarchitectures made of large arrays or ensembles of curved and interconnected nanoelements responsible for the appearance of novel and unusual nanoscale effects have attracted considerable attention due to the vast range of properties and applications in energy storage [1], drug delivery [2], electrocatalysis and sensing [3], advanced magnetic [4], spintronic [5] and superconducting applications [6,7]. Particularly, 3D nanomagnetism involve a large variety of potential applications in multistate memristors [8], thermal energy regulation [9], neuromorphic computing [10], tunable microwave absorption [11], electrochemical devices [12], magnonic conduits [13], domain wall motion memories [14], and spintronics [15,16]. In addition to the widely used top-down manufacturing techniques for the synthesis of 3D nanomaterials with distinct morphologies [17–20], electrochemical deposition (ECD) has been proven to be a versatile, low-cost, and easy-to-implement bottom-up technique that enables the fabrication of a wide range of 3D nanoarchitectures. Specifically, parallel or 3D interconnected nanowire and nanotube networks grown by ECD into the pores of alumina or polymer membranes are interesting materials that are at the center of an intense research activity due to their specific morphological characteristics, magnetic properties and magneto-transport behavior [21–24].

Unlike homogeneous nanowires, nanotubes are interesting nanostructures due to their inner cavity and the possibility of modifying their wall thickness, which confer them an additional morphological characteristic useful to control the magnetic and magneto-transport behavior of the entire nanostructured array [25–29]. In addition to conventional techniques based on gaseous precursors like atomic layer deposition (ALD) and chemical vapor deposition (CVD) used for the fabrication of nanotubes [30,31], an easy and low-cost method based on ECD for the synthesis of large arrays of nanotubes within porous membranes is electrochemical dealloying. This method consists of the dissolution by electrochemical oxidation of the more noble metal located at the core in shell/core nanocables [32]. The use of this method has enabled the synthesis of template-free [33] and template-based parallel Ni nanotubes [25,32–34], and crossed nanotube (NT) networks [27]. Despite

* Corresponding author.
E-mail address: delatorre@materiales.unam.mx (J. de la Torre Medina).

https://doi.org/10.1016/j.jmmm.2026.174081
Received 15 January 2026; Received in revised form 18 March 2026; Accepted 30 March 2026
Available online 30 March 2026
0304-8853/

these advances, arrays of nanotubes made of other magnetic metals have not been reported due to the difficulty of preventing the less noble metal from dissolving during the oxidation process of the more noble metal.

In this study, we exploit this electrochemical dealloying method, previously used only for the fabrication of Ni nanotubes, for the synthesis of NiCo alloy crossed NT networks with precise control over the Co content and their morphological characteristics. It has been found that successful synthesis of NiCo alloys is achieved for Co content up to about 27%, which prevents Co from being removed during the Cu oxidation reaction in the electrochemical dealloying process. The tubular characteristic of synthesized crossed NT networks has been confirmed not only by their morphology but also by their magnetic and magneto-transport behavior. The possibility of manufacturing large ensembles of tubular nanostructures using a low-cost and easy-to-implement technique, such as electrochemical dealloying, paves the way for novel and functional magnetic nano-architectures for sensing, logic gates, and spintronic applications.

2. Materials and methods

2.1. Synthesis of 3D NiCo crossed NT networks

The growth of NiCo crossed NT networks has been carried out by a standard three-probe ECD technique into the interconnected pores of nanoporous polycarbonate (PC) membranes. As shown in Fig. 1(a), the interconnected pore architecture is achieved by exposing a continuous PC film to an irradiation stage at two fixed angles of −25° and +25° in the y-z plane perpendicular to the film plane. These nominal fixed angles have been provided by the manufacturer along with a slight deviation of ±5° [35]. To enlarge the latent tracks to the desired pore diameter of 290 nm, the irradiated PC film was chemically etched in a 0.5 M NaOH aqueous solution at 70 °C [35]. As a result, porous membranes with interconnected pores 290 nm in diameter and volumetric porosity (P) of about 20%, were obtained. Following this procedure, a Cr(10 nm)/Au(2000 nm) layer was evaporated onto one side of the membranes to serve as a cathode for the ECD, as a ground plane for the ferromagnetic resonance (FMR) experiments, and as an electrode for the magnetotransport measurements. NiCo crossed NTs (outer diameter ϕ = 290 nm) were fabricated by following the dealloying process previously reported for arrays of parallel nanowires [25,28,36], and Ni crossed NTs [27]. In this process, shell–core NiCo/Cu nanocables were first grown at a constant deposition potential of −1.1 V, followed by the selective electrochemical etching of the Cu-rich core at an oxidation potential of +0.2 V while keeping intact the NiCo shell. As shown in Table 1, three NiCo crossed NT alloys were fabricated using electrolytes with Co to Co + Ni sulfamate ratios $r = M_{Co}/(M_{Co} + M_{Ni})$ of 5%, 10%, and 20%, where M_{Co} and M_{Ni} represent the molar amounts of Co and Ni sulfamates, respectively.

2.2. Structural characterization and EDX analysis

The porous PC template was removed with dichloromethane to perform the morphology characterization of the NiCo crossed NT networks using a field-emission scanning electron microscope (FE-SEM) JEOL 7600F. The composition of the NiCo crossed NT networks was determined by energy-dispersive X-ray spectroscopy (EDX) analysis, using a JED-2300 Analysis Station FE-SEM. At least 10 EDS mappings at a magnification of X30,000 and acceleration voltage of 15 kV were carried out on each crossed NT network, and the ZAF Method Standardless Quantitative Analysis was used to quantify the amount of atomic % of Ni and Co in the NiCo alloy crossed NT networks.

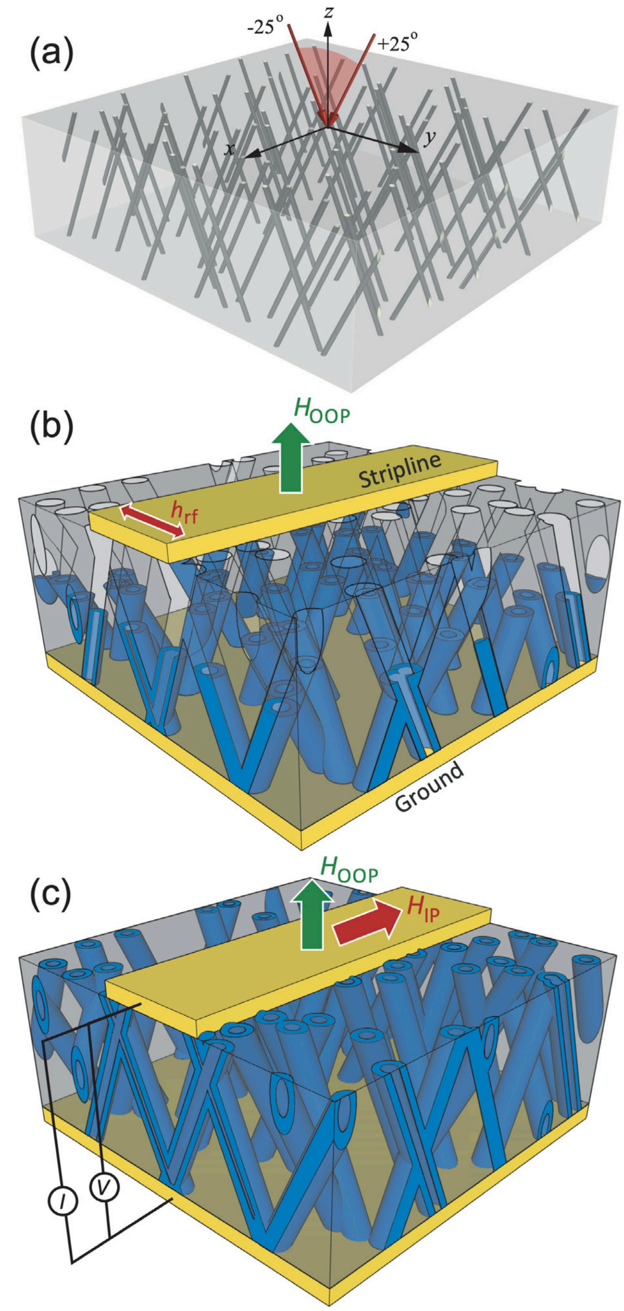

Fig. 1. Schematic representations of (a) the track etching process for the irradiation stage at two fixed angles of −25° and +25° perpendicular to the film plane, (b) the FMR experimental setup composed of the crossed NT network embedded in the porous PC membrane and a microstrip line evaporated onto the top surface of the membrane through which an RF signal is injected, and (c) the two-probe electrode design for magneto-transport measurements in the in-plane (IP) and out-of-plane (OOP) directions of NiCo crossed NT network films.

2.3. Magnetic characterization by AGM and FMR

Magnetization hysteresis loops have been recorded using an alternating gradient magnetometer (AGM) from Lakeshore by applying a maximum applied field of ±14 kOe along the in-plane (IP) and out-of-plane (OOP) directions of the crossed NT network plane. Besides, room temperature ferromagnetic resonance (FMR) spectra have been recorded at a constant excitation frequency in the range of 10 to 32 GHz, by sweeping the magnetic field along the OOP direction from

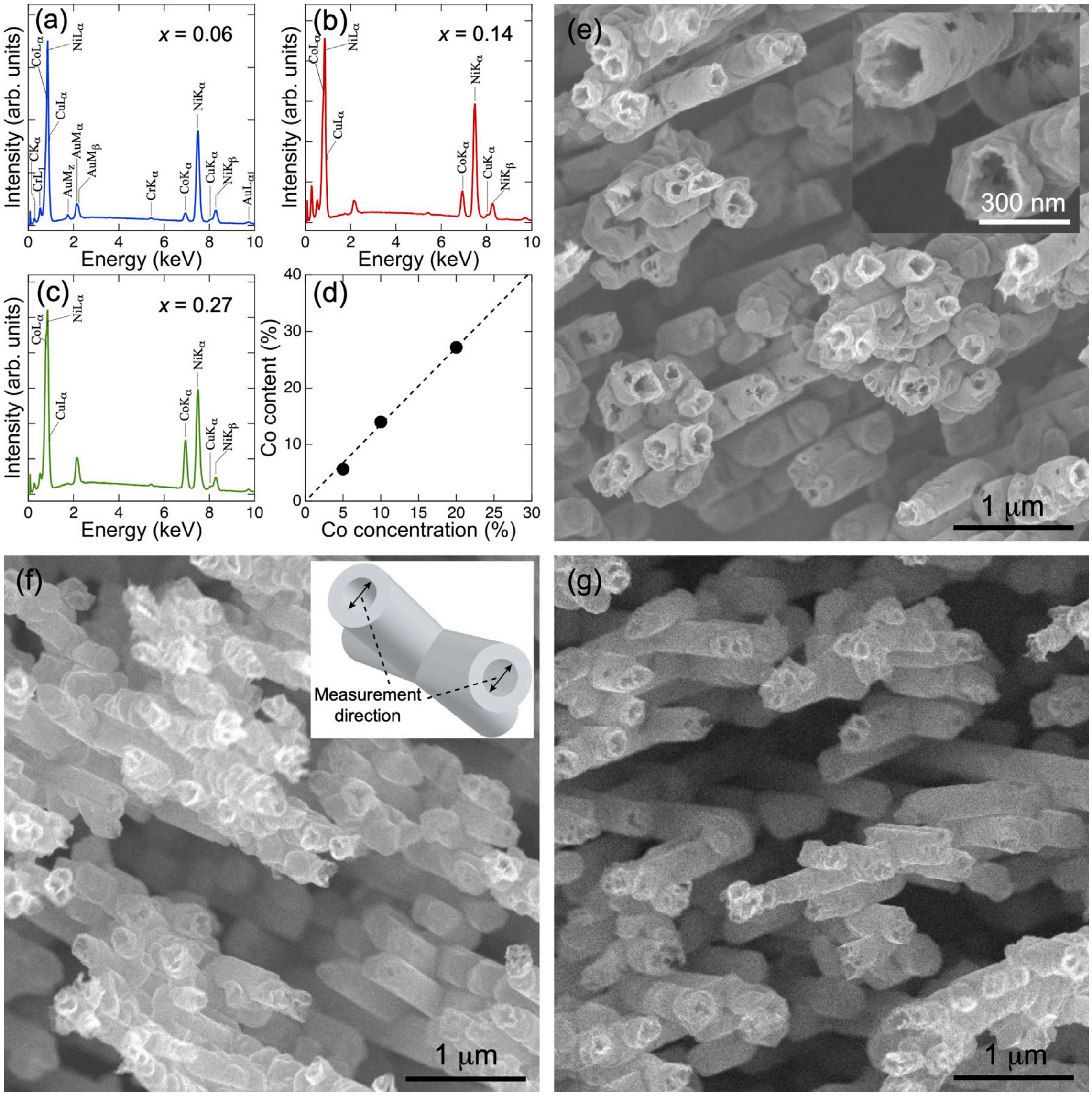

Fig. 2. EDX spectra for $Ni_{1-x}Co_x$ crossed NT networks after completing the dealloying process, corresponding to Co composition values of (a) $x = 0.06$, (b) $x = 0.14$, and (c) $x = 0.27$. (d) Variation in Co content in NiCo alloy NTs as a function of Co concentration in NiCo electrolytic solutions. The dotted line is a linear fit to the data with a slope of 1.36 (content/concentration). FE-SEM micrographs of three interconnected $Ni_{1-x}Co_x$ crossed NT networks with Co contents x of (e) 0.06, (f) 0.14, and (g) 0.27. The inset in (e) shows close details of the crossed NT structure, which allows finding the corresponding inner diameter and an average outer diameter of the nanotubes of about 290 nm. The schematic in (f) indicates the measurement direction of the NTs inner diameter used in their corresponding statistics.

10 kOe down to zero field. As shown in Fig. 1(b), these measurements were carried out using the microstrip line wave-guide configuration, which consists of a 500 μm wide and 500 nm thick metallic microstrip evaporated onto the free side of the porous PC membrane after electrodeposition. Prior to the evaporation of the microstrip line, the crossed NTs growth is stopped before overfilling of the PC membrane to prevent any electrical contact between the NT network and the microstrip.

2.4. Electrical magneto-transport characterization

A two-probe method has been used for magnetoresistance (MR) measurements obtained by sweeping the magnetic field between ±15 kOe. Contrary to the FMR measurement setup, in this case overfilling of the porous PC membranes with crossed NTs has been allowed to have a good electrical contact between the ground plane and the microstrip line, as shown in Fig. 1(c). In this way, the current is injected directly between the two electrodes, taking advantage of the high degree of electrical connectivity of the branched NT structure. The electrical contacts were made using silver paint. In this setup, the resistance was measured within its ohmic resistance range with a resolution of one part in 10^5, which is traduced as an input power that was kept below 0.1 μW to avoid self-heating.

3. Results and discussion

Figs. 2(a)–(c) show the compositional analysis performed by recording EDX spectra for the three NiCo crossed NT networks fabricated using the electrolytes in Table 1 after dissolution of the Cu core. In all cases, the EDX spectra reveal Co and Ni peaks, for which the intensity of the CoK_α peak increases with increasing Co concentration in the electrolyte. Furthermore, the very low intensity CuK_α peak in all the EDX spectra shows that the presence of Cu in the NiCo crossed NT networks is negligible, indicating that the Cu core has been removed.

Table 1
Formulas for electrolytic bath solutions used for the growth of three different crossed NT alloys, taking into account ratios $r = M_{Co}/(M_{Co}+M_{Ni})$ of 5%, 10% and 20%, where M_{Co} and M_{Ni} are the millimolar amounts of Co sulfamate ($Co(H_2NSO_3)_2 \cdot xH_2O$) and Ni sulfamate ($Ni(H_2NSO_3)_2 \cdot 4H_2O$). The same pH value adjusted to 4 and 100 mM and 50 mM of boric acid (H_3BO_3) and Cu sulfate pentahydrate ($CuSO_4 \cdot 5H_2O$), respectively, are used for all the electrolytes.

Reagent	$r = 5\%$	$r = 10\%$	$r = 20\%$
H_3BO_3	100	100	100
$Ni(H_2NSO_3)_2 \cdot 4H_2O$	380	360	320
$Co(H_2NSO_3)_2 \cdot xH_2O$	20	40	80
$CuSO_4 \cdot 5H_2O$	50	50	50

Another peaks corresponding to Cr and Au arise from the evaporated cathode onto the bottom side of the membranes used for growing the crossed networks. The compositional analysis carried out by EDX on the crossed NT networks fabricated using electrolytes with Co to Ni + Co ratios of 5%, 10%, and 20% has revealed alloy compositions $Ni_{1-x}Co_x$ with Co contents x of 6%, 14%, and 27%, respectively. The correspondence between Co content in the alloys and Co concentration in the electrolytes is shown in Fig. 2(d). The linear relationship with a slope of 1.36 (content/concentration) demonstrates that the Co content is higher than expected in the crossed NT-alloy networks. This behavior is in good agreement with previous studies, suggesting that this excess in Co content is due to an anomalous co-deposition in which the reaction rate of the less noble metal (Co) increases at the expense of the reaction rate of Ni, as a result of the higher adsorption ability of Co ions at the cathode diffusion layer promoting inhibition of Ni ions [37–39]. At Co concentrations lower than 30% in the electrolyte, content/concentration ratios greater than one have been reported, with values in the range of 2.1 to 4.8 [37,38,40–43], which, although higher than the value of 1.36 reported in this work, are consistent with anomalous co-deposition behavior. Besides, Figs. 2(e) to (g) show FE-SEM micrographs for the three NiCo crossed NT networks with different alloy compositions after complete dissolution of the PC membrane. As observed, each network exhibits a complex interconnected structure, and the micrographs provide evidence of the fixed angle to about 25° of the crossed NTs with respect to the normal to the membrane plane, as a result of its irradiation to energetic heavy ions in the track etching process. These micrographs confirm the tubular structure of the nanotubes (NTs), and an average outer diameter of 290 ± 15 nm.

Furthermore, a detailed statistical analysis has been carried out on a large number of NTs in each network to determine their inner diameter, which was measured perpendicularly to the NTs tilt angle direction and parallel to the membrane plane, as shown in the inset of Fig. 2(f). The inner diameter of the NTs has been found to depend on the Co content in the alloys, with average values of 155 ± 20 nm, 125 ± 20 nm, and 100 ± 20 nm for the $Ni_{1-x}Co_x$ with $x = 0.06$, 0.14, and 0.27, respectively. This leads to corresponding average NT wall thickness values of 70 ± 10 nm, 85 ± 10 nm, and 95 ± 10 nm. Note that the NT wall thickness for the alloy with the lowest Co content is closer to the average value of about 50 nm reported previously for Ni crossed NTs [27]. The increase in NT wall thickness for NiCo crossed NT networks can be ascribed to the increase in the Co content in the alloys due to the anomalous co-deposition mentioned above, which leads to an increase in the fraction of Ni + Co ad-atoms compared to the fraction of Cu ones during the reduction reaction. This behavior is similar to the wall thickness increase of Ni NTs due to the increase in the reduction potential, which is the result of the preferential growth of Ni compared to Cu [27,32]. Besides, the observed fractures, wrinkles, and folded morphology of the crossed NTs can be attributed to the sudden dissolution of the polymer membrane with dichloromethane, subsequent manipulation, and to its fragility caused by the thin walls of the NTs and their interconnections. This morphological analysis demonstrates the feasibility of synthesizing NiCo 3D crossed NT networks with Co contents of up to 27%, as confirmed by EDX analysis. On the other hand, attempts to grow NiCo NTs with higher Co contents were unsuccessful, which can be ascribed to the simultaneous removal of Cu and Co during the application of the oxidation potential of +0.2 V used to remove the Cu core. Indeed, at high Co concentrations, Co is also removed as a result of the anodic peak associated with Co oxidation at positive potentials in the redox reactions using sulfate-based electrolytes [44]. Therefore, the stability of NiCo crossed nanotubes with low Co contents can be related to the protection conferred by the bulk Ni structure to Co ad-atoms as a result of the Ni protective passive film formed using sulfamate-based electrolytes [45].

The magnetic properties of the NiCo crossed NT networks were first analyzed by recording hysteresis loops at room temperature with the magnetic field applied in the IP and OOP directions, as shown in Fig. 3(a). Magnetic saturation is reached at field values close to 4 kOe, as shown by the full-field hysteresis loops in the inset in the upper left corner. This figure displays the hysteresis loops measured in both directions for the NiCo crossed NT network with $x = 0.27$, whose characteristics are similar to those for the NiCo alloys with lower Co contents. Comparing these hysteresis loops, we observe that the loop in the OOP (IP) direction shows a lower (higher) remanent magnetization (M_r) (see the inset), but faster (slower) saturation. This complex behavior can be attributed to the presence of a combination of vortex (V) and transverse (T) reversal modes, as shown experimentally and validated by an analytical model in a previous work [46], which are different depending on the relative orientation (θ) between the applied field and the nanotube axis. This is, the lower coercive field (H_c) in the OOP direction is consistent with low H_c values due to the V mode, whereas the higher H_c in the IP direction is consistent with high H_c values due to the T mode [46]. According to these results, the V and T modes are dominant at lower and higher θ values [26,47], respectively, as in the case of 25° and 65° corresponding to the OOP and IP direction. Regarding the remanent magnetization, this parameter is lower along the OOP direction than in the IP direction (see the inset of Fig. 3(a)), contrary to what has been reported for low-diameter NTs for which remanence decreases with increasing θ [48]. This discrepancy may be ascribed to the larger outer diameter of the NTs considered in the present work. Figs. 3(b) and (c) show the variation of M_r and H_c as a function of the Co content x in the alloyed $Ni_{1-x}Co_x$ crossed NT networks considered in the present work. As observed, both M_r and H_c are higher along the IP direction regardless of the x value and M_r displays a clearer decreasing behavior with x in the OOP direction than in the IP direction. In Figs. 3(b) and (c), the data obtained on a pure Ni NT network (outer diameter 230 nm) [27], are also reported for comparison.

Besides, recording hysteresis loops along the IP direction reveals a similar magnetic behavior for the three NiCo alloy crossed NT networks, as observed in Fig. 3(d). A slight difference in the saturation field and M_r is evident, so that the larger the M_r, the lower the saturation field for lower Co contents. Note that the shape of all the hysteresis loops in the IP direction close to zero field is very similar, as observed in the inset of Fig. 3(d), which may explain the non-monotonic behavior of both H_c and M_r observed in Figs. 3(b) and (c). More insight into the influence of the Co content on the magnetic behavior can be gained from the hysteresis loops measured along the OOP direction, as shown in Fig. 3(e). In this case, the increase in the Co content is more evident as it leads to appreciable differences in both M_r (see the inset) and the shape of the hysteresis loops with few variations in H_c. Previous results suggest that the decrease in M_r is associated with an increase in the NTs wall thickness in arrays of parallel Ni NTs [25,34] and Ni crossed NT networks [27]. This behavior is in good agreement with the NiCo crossed NT networks of the present work, since lower M_r values are observed for networks with thicker NT walls, as found above by the statistical analysis performed on the FE-SEM micrographs. As pointed out in a previous work, thicker NT walls result in larger dipolar fields

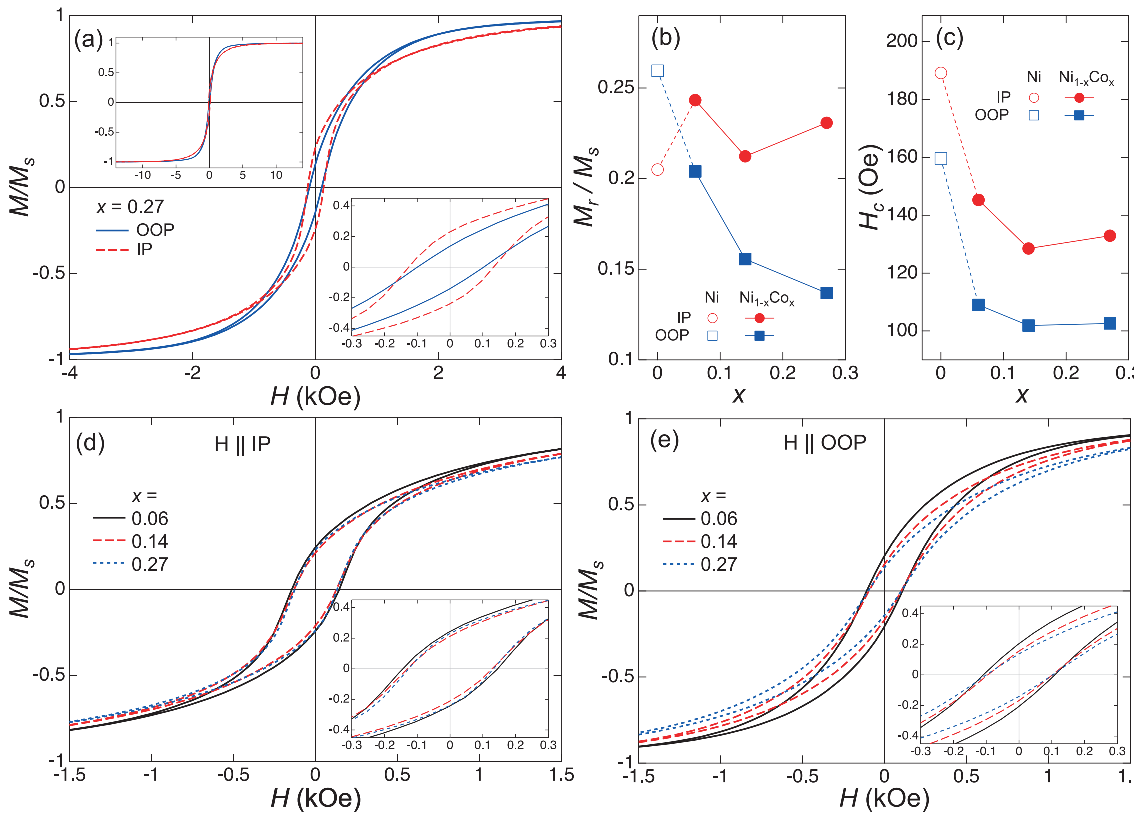

Fig. 3. (a) Hysteresis loops measured with the magnetic field applied along IP (dashed line) and OOP (continuous line) directions of the porous membrane for the NiCo crossed NT network with $x = 0.27$. Variation of (b) the remanent magnetization (M_r/M_s) and (c) the coercive field H_c as a function of the Co content x in $Ni_{1-x}Co_x$ crossed NT networks. Values for M_r/M_s and H_c for the pure Ni crossed NT network (empty symbols) [27], are included for comparison. The dotted and continuous lines are a guide for the eye. (d) Hysteresis loops measured in the IP direction for $Ni_{1-x}Co_x$ crossed NT networks grown using reduction/oxidation potentials of −1.1/+0.2 V with $x = 0.06$ (continuous line), $x = 0.14$ (dashed line), and $x = 0.27$ (dotted line). (e) Corresponding hysteresis loops measured in the OOP direction for the NiCo crossed NT networks in (b). The inset in the upper left corner of (a) shows the corresponding full-field hysteresis loops, whereas the insets in the lower right corners show close views of each figure at low field values.

due to the increasingly closer magnetic poles at the NTs inner surface, which explains the decrease in M_r [27]. However, the demagnetizing field generated between the inner and outer NT surfaces does not necessarily decrease for larger NT walls, because in this case, a larger Co content leads to a higher saturation magnetization. Therefore, the competition between the dipolar and demagnetizing fields may result in a reinforcement of the magnetization easy axis along the OOP direction and the magnetic anisotropy of the crossed NT networks. Hysteresis loops measurements have evidenced the complex magnetic behavior governed by distinct magnetization reversal modes that depend on the measurement direction. These processes can hinder magnetic properties like the preferential orientation of the magnetization of the entire network, as corroborated by the similarity between hysteresis loops measured along the IP and OOP directions shown in Figs. 3(d) and (e).

To overcome this limitation, performing measurements in a saturated state suppresses magnetization reversal processes and provides a better understanding of the magnetic behavior. An adequate measurement technique to perform this kind of analysis is FMR. In this work, NiCo crossed NT networks are expected to be polycrystalline without magnetocrystalline anisotropy contributions as a result of the low Co content, which means that only magnetostatic contributions are considered [49,50]. Fig. 4(a) shows field sweep absorption spectra recorded at $f = 20$ GHz for the three NiCo crossed NT networks with different Co contents x. These spectra are similar to each other and shifted towards lower resonance fields as the Co content increases. Recording FMR spectra at other excitation frequencies allows obtaining the dispersion relations shown as symbols in Figs. 4(b) - (d) for each crossed NT network. As observed, all fitted dispersion relations using

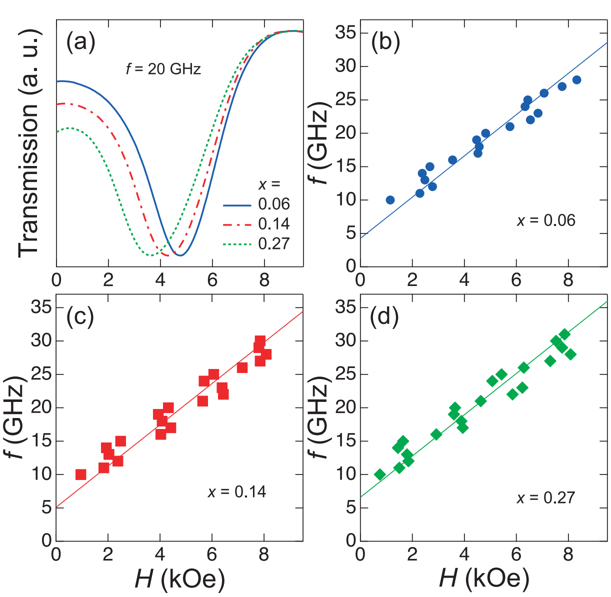

Fig. 4. (a) FMR spectra recorded at $f = 20$ GHz on $Ni_{1-x}Co_x$ crossed NT networks with Co contents of 6%, 14%, and 27%. Dispersion relations for (b) $x = 0.06$, (c) $x = 0.14$, and (d) $x = 0.27$. The continuous lines in (b)–(d) are fits to the data using the FMR condition of Eq. (1).

Eq. (1) display a positive zero intercept, indicating positive anisotropy or preferential magnetization orientation along the OOP direction. Furthermore, dispersion relations for NiCo crossed NT networks with higher x values are shifted towards higher resonance frequencies, consistent with the increase in the saturation magnetization. Additionally, a quantitative analysis is needed to explain the shift in the relation dispersions towards higher resonance frequencies resulting from the rise in Co content. The crossed NT networks correspond to ensembles of tilted cylindrical nanostructures with uniaxial anisotropy that replicate the porous architecture of the membrane and span along the y direction with fixed polar orientation angle θ with respect to the OOP direction. Therefore, the FMR resonance condition in the saturated state for a purely magnetostatic system with dominant uniaxial anisotropy, obtained using the Smit and Beljers formalism, reads [51,52]

$$\left(\frac{f}{\gamma}\right)^2 = \left(H_r + H_{eff}\cos 2\theta\right)\left(H_r + H_{eff}\cos^2\theta\right), \quad (1)$$

where f is the excitation frequency, γ is the gyromagnetic ratio of about 3.09 GHz kOe^{-1} for Ni rich NiCo alloys, H_{eff} is the effective anisotropy field, and H_r is the resonance field. In this equation, θ is the angle for the saturated magnetization along the applied field parallel to the OOP direction, measured with respect to the nanotube axis. The resonance condition serves as a fitting function for the f vs H dispersion relation of each crossed NT network, determining its corresponding effective field. When comparing Figs. 4(b), (c), and (d), it can be seen that the resonance frequency extrapolated to zero field (f_0) increases as the Co content x increases. Therefore, setting $H_r = 0$ in Eq. (1) leads to a simple expression for H_{eff} in terms of the experimental f_0 value, this is

$$H_{eff} = \frac{f_0}{\gamma\cos\theta\sqrt{\cos 2\theta}}, \quad (2)$$

where $\theta = 25°$ for the crossed NT networks of this work. Using Eq. (2) to obtain H_{eff} leads to values of 1.88 ± 0.27, 2.24 ± 0.32, and 2.96 ± 0.43 kOe for $x = 0.06$, 0.14, and 0.27, respectively. As predicted by the Slater-Pauling curve, increasing the Co content in NiCo alloys leads to an increase in the saturation magnetization (M_s) [53]. Therefore, the increase in H_{eff} is due to the increase in M_s because of the proportionality between both parameters. Furthermore, this result shows that the decrease in the remanent magnetization along the OOP direction with increasing the Co content x (see Figs. 3(b) and (e)), does not have a significant influence on H_{eff}.

Magneto-transport measurements have been performed to further investigate the magnetic behavior of NiCo crossed NT networks. Anisotropic magnetoresistance (AMR) measurements yield variations in the electrical resistance (R) as a result of changes in the relative orientation between the magnetization (M) and the electrical current (I). Figs. 5(a) and (b) show magnetoresistance curves for $Ni_{1-x}Co_x$ crossed NT networks with $x = 0.06$ and $x = 0.27$, respectively, measured with the magnetic field applied along the IP (dotted lines) and OOP (continuous lines) directions of the porous membrane plane. These curves exhibit the characteristic bell-shape typical of the AMR effect and provide useful information from both the saturated magnetic state and in the vicinity of zero field. In the saturated state ($H = \pm 15$ kOe) along the IP and OOP directions, M and I are at the fixed angles of 65° and 25° with respect to each other, respectively. In this configuration, the AMR ratio or fractional increase in R ($\Delta R/R$) can be obtained from the resistivity values at saturation ρ_{ip} and ρ_{oop}, which depend on the resistance states for which M is parallel ($\rho_\parallel$) and perpendicular ($\rho_\perp$) to I [49], that is

$$\frac{\Delta\rho}{\rho} = \frac{\rho_\parallel - \rho_\perp}{\rho_{av}}, \quad (3)$$

where $\rho_{av} = (\rho_\parallel + 2\rho_\perp)/3$ is the average magnetoresistance in 3D networks and $\rho_\parallel = \rho_{ip} + \rho_{oop} - \rho_\perp$ and $\rho_\perp = (k\rho_{ip} - (1-k)\rho_{oop})/(2k-1)$ [27]. Applying Eq. (3) to the magnetoresistance curves in Figs. 5(a) and (b) leads to AMR ratios of about 1.50% and 0.43% for $x = 0.06$ and

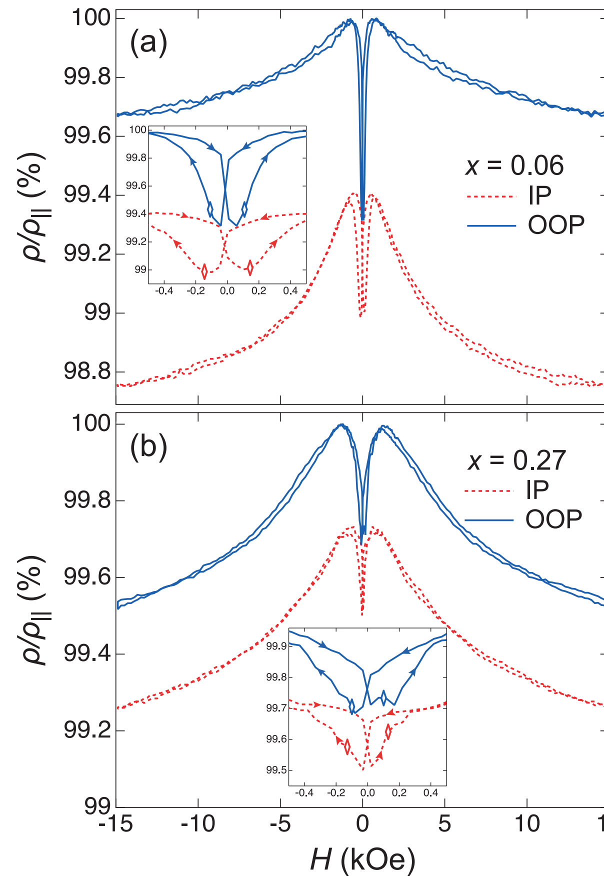

Fig. 5. Magnetoresistance curves measured with the magnetic field applied along the IP (dotted lines) and OOP (continuous lines) directions to the plane of the porous template for two $Ni_{1-x}Co_x$ crossed NT networks with (a) $x = 0.06$ and (b) 0.27. The insets show close details of the IP and OOP magnetoresistance curves in the vicinity of zero field, where arrows indicate the direction of the magnetic field sweep for both positive to negative and negative to positive branches. The lozenges represent the resistance states at the coercive field for each network.

$x = 0.27$, respectively. This decrease in $\Delta R/R$ with x is due to the decrease in the effective magnetic moment per atom and consistent with previous results for NiCo alloys made as thin films [49] and nanowires [50,54]. On the other hand, the magnetoresistance curves in the IP and OOP directions are different from the expected bell-shape of the AMR effect as a result of the presence of a resistance drop in the vicinity of zero field, as seen in Fig. 5. As suggested previously by experimental evidence and micromagnetic simulations, this behavior originates from magnetization reversal processes where vortex-like domain walls are propagated, which are more likely in magnetic NTs as a result of their hollow feature [29,55]. Other previous works also suggest that the curling (vortex) reversal mode and the propagation of vortex domain walls are the dominant reversal mechanisms in tilted magnetic NTs [46,56]. The combination of bell-shaped curves and the resistance drop suggests similar magnetization reversal processes in both IP and OOP directions originated from the corresponding tilt angle of the NTs. However, the resistance drops near zero field for the NiCo crossed NT network with $x = 0.06$ is deeper and closer to zero field along the OOP direction, which is consistent with a faster magnetization reversal as suggested by the lower coercive field in this direction (see Fig. 3(c)). This discrepancy between the IP and OOP resistance drop minima reflects the magnetic anisotropy for this network, which is consistent with the comparison between hysteresis loops in Figs. 3(d) and (e). Therefore, the fast resistance drop near zero field and the large discrepancy between the IP and OOP curves, attributed respectively to the vortex-like reversal process and the strong magnetic anisotropy, are characteristics typical of Ni-rich crossed NT networks. Indeed, previous results on pure Ni crossed NT networks are in good agreement with this scenario [27].

Besides, the minimum in the resistance drop is ascribed to the material demagnetized state reached at the coercive field for which the resistance state is independent of the magnetization [57]. The insets in Figs. 5(a) and (b) display close details of the resistance drops near zero field in each applied field direction. In these figures, the coercive field position is represented by lozenges on the resistance curves. As a general trend, the symbols are close to the resistance minima for both NiCo alloys, except for the NiCo alloy with $x = 0.27$ along the IP direction. This discrepancy can be related to the thicker crossed NT walls, which may be responsible for the nucleation of larger magnetic domains that propagate via magnetization reversal modes other than curling or vortex. Particularly, the magnetoresistance curves in the IP and OOP directions for the crossed NT network with $x = 0.27$ are close and similar to each other, suggesting an almost isotropic magnetic behavior, consistent with the hysteresis loops shown in Fig. 3(a). This behavior explains the similar resistance drop minimum and coercive field values in the IP and OOP directions for this crossed NT network. Finally, these properties are of significant technological and research interest, suitable for the development of device applications based on nanoscale materials with tunable magnetic and magneto-transport behavior.

4. Conclusions

In this work, we successfully synthesized large-scale NiCo alloy crossed NT networks using track-etched PC membranes with interconnected cylindrical nanopores and studied their magnetic and magneto-transport behavior. We demonstrated that the electrochemical dealloying technique, which consists of removing the Cu core from core/shell nanowires where the shell is formed of a magnetic material, and which had previously only been demonstrated for the fabrication of pure Ni nanotubes, could also be extended to the fabrication of NiCo alloy nanotubes with Co contents of up to around 27%. Furthermore, it has been shown that it is possible to achieve precise control over the composition of Ni-rich NiCo crossed NT networks and the thickness of the tube walls, offering the possibility of controlling their magnetic behavior. Within the considered range of alloy compositions in this work, a straightforward linear relationship between the Co content in the alloys and the Co composition in the electrolytes has been found, which is useful for accurately predicting any alloy composition. It has been found that increasing the alloys Co content causes an increase in the nanotubes wall thickness and in the magnetic anisotropy field, as determined by FMR experiments. For all the alloys, the magneto-transport behavior is consistent with the propagation of vortex-like domain walls during magnetization reversal. Furthermore, the increase in the Co content leads to a decrease in the AMR ratio, consistent with previous reports, and the magnetization reversal process has been closely related to the crossed NT networks coercivity. The results discussed in the present study expand the knowledge on the use of the electrochemical dealloying technique for obtaining NiCo alloy nanotubes. Finally, these findings are of special interest for the development of potential devices and technological applications involving interconnected nanotubes with tunable morphology, materials, and magnetic and magneto-transport behavior.

CRediT authorship contribution statement

Joaquín de la Torre Medina: Writing – review & editing, Writing – original draft, Visualization, Validation, Supervision, Methodology, Investigation, Formal analysis, Data curation, Conceptualization. **Pascal Van Velthem:** Validation, Methodology, Investigation, Data curation. **Tristan da Câmara Santa Clara Gomes:** Writing – review & editing, Validation, Formal analysis. **Flavio Abreu Araujo:** Validation, Software, Methodology. **Luc Piraux:** Writing – review & editing, Supervision, Resources, Methodology, Funding acquisition, Formal analysis.

Declaration of competing interest

The authors declare that they have no known competing financial interests or personal relationships that could have appeared to influence the work reported in this paper.

Acknowledgments

This work was partly supported by the 2025 UNAM-DGAPA-PAPIIT Program project IN106025. Financial support was also provided by the Belgian Fund for Scientific Research (F.R.S.-FNRS). F.A.A. is a Research Associate of the F.R.S.-FNRS. Financial support was provided by the European Union. Views and opinions expressed are however those of the authors only and do not necessarily reflect those of the European Union or the European Research Executive Agency (REA). Neither the European Union nor the granting authority can be held responsible for them. T.d.C.S.C.G. is an ERA fellow.

Data availability

Data will be made available on request.

References

[1] Nisha Loura, Sumit Mor, Deepak Nandal, Vikas Nandal, Vikas Dhull, Synthesis strategies of smart 3d nanoarchitectures and their applications in energy storage and conversion, Energy Storage 6 (1) (2024) e559.
[2] G. Gunkel-Grabole, S. Sigg, M. Lomora, C.G. Palivan S. Lörcher, W.P. Meier, Polymeric 3D nano-architectures for transport and delivery of therapeutically relevant biomacromolecules, Biomater. Sci. 3 (1) (2015) 25–40.
[3] Ye Ji Kim, Gyu Rac Lee, Eugene N Cho, Yeon Sik Jung, Fabrication and applications of 3d nanoarchitectures for advanced electrocatalysts and sensors, Adv. Mater. 32 (35) (2020) 1907500.
[4] Oleksandr V. Dobrovolskiy, Oleksandr V. Pylypovskyi, Luka Skoric, Amalio Fernández-Pacheco, Arjen Van Den Berg, Sam Ladak, Michael Huth, Complex-shaped 3D nanoarchitectures for magnetism and superconductivity, in: Curvilinear Micromagnetism, Springer, Cham, Switzerland, 2022, pp. 215–268.
[5] Gianluca Gubbiotti, Anjan Barman, Sam Ladak, Cristina Bran, Dirk Grundler, Michael Huth, Harald Plank, Georg Schmidt, Sebastiaan van Dijken, Robert Streubel, Oleksandr Dobrovoloskiy, Valerio Scagnoli, Laura Heyderman, Claire Donnelly, Olav Hellwig, Lorenzo Fallarino, M. Benjamin Jungfleisch, Alan Farhan, Nicolò Maccaferri, Paolo Vavassori, Peter Fischera, Riccardo Tomasello, Giovanni Finocchio, Rodolphe Cléraca, Roberta Sessoli, Denys Makarov, Denis D. Sheka, Maciej Krawczyk, Rodolfo Gallardoa, Pedro Landeros, Massimiliano D'Aquino, Riccardo Hertel, Philipp Pirro, Florin Ciubotaru, Markus Becherer, Jack Gartside, Teruo Ono, Paolo Bortolotti, Amalio Fernández-Pacheco, 2025 roadmap on 3D nanomagnetism, J. Phys. : Condens. Matter 37 (14) (2025) 143502.
[6] Denys Makarov, Oleksii M. Volkov, Attila Kákay, Oleksandr V. Pylypovskyi, Barbora Budinská, Oleksandr V. Dobrovolskiy, New dimension in magnetism and superconductivity: 3D and curvilinear nanoarchitectures, Adv. Mater. 34 (3) (2022) 2101758.
[7] Vladimir M. Fomin, Oleksandr V. Dobrovolskiy, A perspective on superconductivity in curved 3D nanoarchitectures, Appl. Phys. Lett. 120 (9) (2022).
[8] Dhritiman Bhattacharya, Zhijie Chen, Christopher J. Jensen, Chen Liu, Edward C. Burks, Dustin A. Gilbert, Xixiang Zhang, Gen Yin, Kai Liu, 3D interconnected magnetic nanowire networks as potential integrated multistate memristors, Nano Lett. 22 (24) (2022) 10010–10017.
[9] Muhammad Maqbool, Akbar Bashir, Ali Usman, Muhammad Khurram, Waseem Aftab, Yongliang Li, Ruqiang Zou, 3D interconnected boron nitride macrostructures and derived composites for thermal energy regulation, Adv. Funct. Mater. 35 (9) (2025) 2414042.
[10] Dhritiman Bhattacharya, Colin Langton, Md Mahadi Rajiba, Erin Marlowea, Zhijie Chen, Walid Al Misba, Jayasimha Atulasimha, Xixiang Zhanga, Gen Yin, Kai Liu, Self-assembled 3D interconnected magnetic nanowire networks for neuromorphic computing, ACS Appl. Mater. Interfaces 17 (13) (2025) 20087–20095.

[11] Chuyang Liu, Lin Zhu, Shiqi Zheng, Lu Xu, Liang Yan, Yujing Zhang, Guangbin Ji, A novel elastic dome array structure for precise pressure regulation toward tunable microwave absorption, Acta Mater. 296 (2025) 121255.

[12] Mahdi Hamidinejad, Heng Wang, A. Sanders Kate, Michael De Volder, Electrochemically responsive 3d nanoarchitectures, Adv. Mater. 36 (2) (2024) 2304517.

[13] Sebastian Lamb-Camarena, Fabrizio Porrati, Alexander Kuprava, Qi Wang, Sven Barth Michal Urbánek, Denys Makarov, Michael Huth, Oleksandr V. Dobrovolskiy, 3D magnonic conduits by direct write nanofabrication, Nanomaterials 13 (13).

[14] Y.M. Hung, T. Li, R. Hisatomi, Y. Shiota, T. Moriyama, T. Ono, Low current driven vertical domain wall motion memory with an artificial ferromagnet, J. Magn. Soc. Jpn. 45 (1) (2021) 6–11.

[15] Oleksii M. Volkova, Oleksandr V. Pylypovskyi, Fabrizio Porrati, Florian Kronast, Jose A. Fernandez-Roldan, Attila Kákay, Alexander Kupravaa, Sven Barth, Filipp N. Rybakov, Olle Eriksson, Sebastian Lamb-Camarenaa, Pavlo Makushko, Mohamad-Assaad Mawass, Shahrukh Shakeel, Oleksandr V. Dobrovolskiy, Michael Huth, Denys Makarov, Three-dimensional magnetic nanotextures with high-order vorticity in soft magnetic wireframes, Nat. Commun. 15 (2193) (2024) 1–13.

[16] Yuxiang Yin, Bingyan Liu, Yaochen Han, Qiling Liu, Jiehao Kou, Yueqi Zhang, Ji Wen, Shihao Liu, Qingyan Wang, Yaotao Shana, Yizhou Liu, Jicheng Feng, Nanoscale 3D printing for empowering future nanodevices, Adv. Mater. Technol. 10 (14) (2025) 2500083.

[17] Sang-Hyeon Nam, Gayea Hyun, Donghwi Cho, Seonggon Hana, Gwangmin Bae, Haomin Chen, Kisun Kim, Youngjin Ham, Junyong Park, Seokwoo Jeon, Fundamental principles and development of proximity-field nanopatterning toward advanced 3D nanofabrication, Nano Res. 14 (9) (2021) 2965–2980.

[18] Xianglong Lyu, Zhiqiang Zheng, Anitha Shiva, Mertcan Han, Cem Balda Dayan, Mingchao Zhang, Metin Sitti, Capillary trapping of various nanomaterials on additively manufactured scaffolds for 3D micro-/nanofabrication, Nat. Commun. 15 (1) (2024) 1–11.

[19] Sabri Koraltan, Fabrizio Porrati, Robert Kraft, Sven Barth, Markus Weigand, Claas Abert, Dieter Suessa, Michael Huth, Sebastian Wintz, Reconfigurable 3D magnetic nanoarchitectures, Adv. Funct. Mater. (2025) e15338, n/a(n/a).

[20] Elina Zhakina, Luke Alexander Turnbull, Weijie Xua, Markus Königa, Paul Simon, Wilder Carrillo-Cabrera, Amalio Fernández-Pacheco, Uri Vool, Dieter Suess, Claas Abert, Vladimir M. Fomin, Claire Donnelly, Reconfigurable three-dimensional superconducting nanoarchitectures, Adv. Funct. Mater. (2025) 2506057, n/a(n/a).

[21] Edward C. Burks, Dustin A. Gilbert, Peyton D. Murray, Chad Flores, Thomas E. Felter, Supakit Charnvanichborikarn, Sergei O. Kucheyev, Jeffrey D. Colvina, Gen Yin, Kai Liu, 3D nanomagnetism in low density interconnected nanowire networks, Nano Lett. 21 (1) (2021) 716–722.

[22] Alejandra Ruiz-Clavijo, Olga Caballero-Calero, David Navas, A. Amanda, Ordoñez-Cencerrado, Javier Blanco-Portals, Francesca Peiró, Ruy Sanz, Marisol Martın-González, Unveiling the complex magnetization reversal process in 3D nickel nanowire networks, Adv. Electron. Mater. 8 (10) (2022) 2200342.

[23] Arturo Galindo, José Luis Reyes-Rodrıguez, Cristian Botez, Mario Moreno, Arturo Ponce, Towards three-dimensional nanoarchitectures: highly ordered bi-layer assembly of tailored magnetic nanowire arrays via template-assisted electrodeposition, Mater. Adv. 3 (11) (2022) 4548–4555.

[24] Qin Xu, Yujie Zhang, Yongna Xiao, Jiayuan Yin, Magnetic properties of bamboo-like Ni-Zn-in nanowires using 3D-AAO templates, Vacuum 230 (2024) 113694.

[25] Y Velázquez-Galván, J M Martínez-Huerta, J de la Torre Medina, Y Danlée, L Piraux, A Encinas, Dipolar interaction in arrays of magnetic nanotubes, J. Phys.: Condens. Matter. 26 (2) (2014) 026001.

[26] M.P. Proenca, C.T. Sousa, J. Escrig, J. Ventura, M. Vazquez, J.P. Araujo, Magnetic interactions and reversal mechanisms in Co nanowire and nanotube arrays, J. Appl. Phys. 113 (9) (2013) 093907.

[27] Joaquın de la Torre Medina, Tristan da Câmara Santa Clara Gomes, G. Yenni, Velázquez Galván, Luc Piraux, Large-scale 3-D interconnected Ni nanotube networks with controlled structural and magnetic properties, Sci. Rep. 8 (14555) (2018) 1–11.

[28] Qingtao Wang, Guanzhong Wang, Xinhai Han, Xiaoping Wang, J.G. Hou, Controllable template synthesis of ni/cu nanocable and ni nanotube arrays: A one-step coelectrodeposition and electrochemical etching method, J. Phys. Chem. B 109 (49) (2005) 23326–23329, PMID: 16375302.

[29] Abhishek Kumar, Chirag Kalouni, Raghvendra Posti, Vivek K. Malik, Dhananjay Tiwari, Debangsu Roy, Unveiling magnetic states in nanotubes: insights from remanent ferromagnetic resonance spectroscopy, Phys. Scr. 100 (3) (2025) 035953.

[30] Maria Carmen Giordano, Simon Escobar Steinvall, Sho Watanabe, Anna Fontcuberta i Morral, Dirk Grundler, Ni 80 Fe 20 nanotubes with optimized spintronic functionalities prepared by atomic layer deposition, Nanoscale 13 (31) (2021) 13451–13462.

[31] Ajeng Eliyana, Rustan Ruslan, Aveni Christy Keintjem, Jasruddin Daud Malago, Toto Winata, The effect of substrate temperature on CNT deposition with Ni catalyst as precursor, J. Phys. Conf. Ser. 2980 (1) (2025) 012007.

[32] Zhu Liu, Guoqiang Xia, Frank Zhu, Su Kim, Nina Markovica, Chia-Ling Chien, Peter C. Searson, Exploiting finite size effects in a novel core/shell microstructure, J. Appl. Phys. 103 (6) (2008) 064313.

[33] Zhe Li, Haidong Bian, Christopher M. Lee, Xiaobo Chen, Yang Yang Li, Nickel nanotube array via electroplating and dealloying, Thin Solid Films 658 (2018) 1–6.

[34] Qingtao Wang, Guanzhong Wang, Xinhai Han, Xiaoping Wang, J.G. Hou, Controllable template synthesis of Ni/Cu nanocable and Ni nanotube arrays: A one-step coelectrodeposition and electrochemical etching method, J. Phys. Chem. B 109 (49) (2005) 23326–23329.

[35] E. Ferain, R. Legras, Track-etch templates designed for micro- and nanofabrication,nuclear instruments and methods in physics research section b: beam interactions with materials and atoms, Ioniz. Radiat. Polym. 208 (2003) 115–122, (Supplement C).

[36] Zhu Liu, Guoqiang Xia, Frank Zhu, Su Kim, Nina Markovic, Chia-Ling Chien, Peter C. Searson, Exploiting finite size effects in a novel core/shell microstructure, J. Appl. Phys. 103 (6) (2008) 064313.

[37] Guiying Qiao, Tianfu Jing, Nan Wang, Yuwei Gao, Xin Zhao, Jifeng Zhou, Wei Wang, High-speed jet electrodeposition and microstructure of nanocrystalline Ni–Co alloys, Electrochim. Acta 51 (1) (2005) 85–92.

[38] Liping Wanga, Yan Gao, Qunji Xue, Huiwen Liu, Tao Xu, Microstructure and tribological properties of electrodeposited Ni–Co alloy deposits, Appl. Surf. Sci. 242 (3) (2005) 326–332.

[39] Abdossalam Karimzadeh, Mahmood Aliofkhazraei, Frank C. Walsh, A review of electrodeposited Ni-Co alloy and composite coatings: Microstructure, properties and applications, Surf. Coat. Technol. 372 (2019) 463–498.

[40] Liangliang Tian, Jincheng Xu, Chengwen Qiang, The electrodeposition behaviors and magnetic properties of Ni–Co films, Appl. Surf. Sci. 257 (10) (2011) 4689–4694.

[41] C. Lupi, A. Dell'Era, M. Pasquali, P. Imperatori, Composition, morphology, structural aspects and electrochemical properties of Ni–Co alloy coatings, Surf. Coat. Technol. 205 (23) (2011) 5394–5399.

[42] M. Zamani, A. Amadeh, S.M. Lari Baghal, Effect of co content on electrodeposition mechanism and mechanical properties of electrodeposited Ni–Co alloy, Trans. Nonferr. Met. Soc. China 26 (2) (2016) 484–491.

[43] Gang Wu, Ning Li, Derui Zhou, Kurachi Mitsuo, Electrodeposited Co–Ni–Al2o3 composite coatings, Surf. Coat. Technol. 176 (2) (2004) 157–164.

[44] M.R. Khelladi, L. Mentar, M. Boubatra, A. Azizi, A. Kahoul, Early stages of cobalt electrodeposition on FTO and n-type si substrates in sulfate medium, Mater. Chem. Phys. 122 (2) (2010) 449–453.

[45] Li Sun, Chia-Ling Chien, Peter C. Searson, Fabrication of nanoporous nickel by electrochemical dealloying, Chem. Mater. 16 (16) (2004) 3125–3129.

[46] Ole Albrecht, Robert Zierold, Sebastián Allendea, Juan Escrig, Christian Patzig, Bernd Rauschenbacha, Kornelius Nielsch, Detlef Görlitz, Experimental evidence for an angular dependent transition of magnetization reversal modes in magnetic nanotubes, J. Appl. Phys. 109 (9) (2011) 093910.

[47] Yu P. Ivanova, M . Vázquez, O. Chubykalo-Fesenko, Magnetic reversal modes in cylindrical nanowires, J. Phys. D: Appl. Phys. 46 (48) (2013) 485001.

[48] Diego Salazar-Aravena, Juan Luis Palma, Juan Escrig, Angular dependence of the magnetic properties of cylindrical nanostructures with wire–tube morphology, Mater. Res. Express 1 (2) (2014) 026112.

[49] T. McGuire, R. Potter, Anisotropic magnetoresistance in ferromagnetic 3d alloys, IEEE Trans. Magn. 11 (4) (1975) 1018–1038.

[50] Tristan da Câmara Santa Clara Gomes, Joaquın De La Torre Medina, Matthieu Lemaitre, Luc Piraux, Magnetic and magnetoresistive properties of 3D interconnected NiCo nanowire networks, Nanoscale Res. Lett. 11 (1) (2016) 1–7.

[51] Carmine Vittoria, Microwave Properties of Magnetic Films, World Scientific, Singapore, 1993.

[52] M. Demand, A. Encinas-Oropesa, S. Kenane, U. Ebels, I. Huynen, L. Piraux, Ferromagnetic resonance studies of nickel and permalloy nanowire arrays, J. Magn. Magn. Mater. 249 (1) (2002) 228–233.

[53] B.D. Cullity, C.D. Graham, Introduction to Magnetic Materials, second ed., Wiley-IEEE Press, 2009.

[54] Takeshi Ohgai, Yuki Ikeda, Takumi Egawaa, Keizo Takao, Masumi Nakai, Shunji Hasuo, Anisotropic magnetoresistance of Ni-Co-Fe alloy nanowires electrodeposited into anodized aluminium oxide membrane thin films, ECS Trans. 50 (10) (2013) 217.

[55] Dhananjay Tiwari, Martin Christoph Scheuerlein, Mahdi Jaber, Eric Gautier, Laurent Vila, Jean-Philippe Attané, Michael Schöbitza, Aurelien Massebœuf, Tim Hellmann, Jan P Hofmanna, Wolfgang Ensinger, Olivier Fruchart, Electrical characterization of the azimuthal anisotropy of (NixCo1-x)B-based ferromagnetic nanotubes, J. Magn. Magn. Mater. 575 (2023) 170715.

[56] J. Escrig, M. Daub, P. Landeros, K. Nielsch, D. Altbir, Angular dependence of coercivity in magnetic nanotubes, Nanotechnology 18 (44) (2007) 445706.

[57] Jehyun Lee, Dieter Suess, Thomas Schrefl, Kyu Hwan Oh, Josef Fidler, Magnetic characteristics of ferromagnetic nanotube, J. Magn. Magn. Mater. 310 (2007) 2445–2447, (2, Part 3).